

Highly efficient luminescent solar concentrators based on earth-abundant indirect-bandgap silicon quantum dots

Francesco Meinardi^{1,2,*†}, Samantha Ehrenberg^{3†}, Lorena Dhamo¹, Francesco Carulli¹, Michele Mauri^{1,2}, Francesco Bruni^{1,2}, Roberto Simonutti¹, Uwe Kortshagen^{3*} and Sergio Brovelli^{1,2*}

Building-integrated photovoltaics is gaining consensus as a renewable energy technology for producing electricity at the point of use. Luminescent solar concentrators (LSCs) could extend architectural integration to the urban environment by realizing electrode-less photovoltaic windows. Crucial for large-area LSCs is the suppression of reabsorption losses, which requires emitters with negligible overlap between their absorption and emission spectra. Here, we demonstrate the use of indirect-bandgap semiconductor nanostructures such as highly emissive silicon quantum dots. Silicon is non-toxic, low-cost and ultra-earth-abundant, which avoids the limitations to the industrial scaling of quantum dots composed of low-abundance elements. Suppressed reabsorption and scattering losses lead to nearly ideal LSCs with an optical efficiency of $\eta = 2.85\%$, matching state-of-the-art semi-transparent LSCs. Monte Carlo simulations indicate that optimized silicon quantum dot LSCs have a clear path to $\eta > 5\%$ for 1 m^2 devices. We are finally able to realize flexible LSCs with performances comparable to those of flat concentrators, which opens the way to a new design freedom for building-integrated photovoltaics elements.

The continuous increase in performance of silicon-based photovoltaic (Si-PV) systems and the economic incentive programmes that have characterized the fiscal policies of many western countries have rendered Si-PVs the dominant technology for producing electrical energy from renewable sources in sustainable civil and industrial buildings. Furthermore, in the last few years, the retail cost of Si-PV modules has dropped by $\sim 70\%$, which now makes it possible to recover the economic investment for rendering a small building energetically independent in less than a decade¹. However, the situation is radically different in highly urbanized environments, where architecture develops predominantly in terms of height, and the rooftop surfaces commonly used for the installation of Si-PV modules become increasingly insufficient to collect all the energy required for building operations. At present, an area of $\sim 7\text{ m}^2$ is needed for 1 kW of peak power. This makes it more difficult to achieve the desired goal of the so-called ‘nearly zero energy building’ decreed by the EU, according to which all newly constructed buildings will be required to be energetically neutral by 2020 (ref. 2). Hence, it is of growing relevance to realize innovative PV systems that integrate into existing and newly constructed buildings without altering their aesthetic appearance or affecting the quality of life of their occupants.

Luminescent solar concentrators (LSCs)^{3,4} could help achieve this goal by transforming conventional energy-passive glazing systems into semi-transparent PV windows⁵, effectively converting the facades of urban buildings into distributed energy generation units^{6–9}. Importantly, integrating LSCs ‘invisibly’ into urban environments would facilitate the public acceptance of PV power and enable seamless integration in this territory, essentially reducing to zero the so-called ‘cost of land’ for PV installation.

A typical LSC consists of a plastic optical waveguide doped with fluorophores or of a glass slab coated with active layers of emissive

materials. Direct, as well as the diffused sunlight that penetrates the matrix, is absorbed by the fluorophores and is re-emitted at a longer wavelength. The luminescence, guided by total internal reflection, propagates to the waveguide edges, where it is converted into electricity by small PV cells installed along the slab perimeter (Fig. 1a). Because the LSC area exposed to sunlight is much larger than the waveguide edges, LSCs can, in principle, greatly increase the flux of radiation incident onto the perimeter PV devices and thus boost the photocurrent^{4,6}. Importantly for building-integrated PV (BIPV) applications, LSCs can be produced with unmatched design freedom in terms of shape, transparency, colour and flexibility, which architects can use to enhance a building’s aesthetic value. In addition to this, the LSC design uniquely enables the harvest of solar radiation using electrode-less semitransparent waveguides, with essentially no aesthetic impact^{7–11}, which is paramount for the realization of PV windows. Finally, because the perimeter PV cells are indirectly illuminated by luminescence originating across the whole waveguide, LSCs are essentially unaffected by the efficiency losses and electrical stresses caused by shadowing of the device that occur in bulk and thin-film PVs.

Despite tremendous advancements in device design^{6,10–12}, the wide use of LSCs has long been hindered by the lack of suitable emitters. Organo-metallic chromophores suffer from limited spectral coverage, while organic dyes and conventional core-only colloidal quantum dots^{13,14} exhibit a large overlap between the absorption and emission spectra, which leads to strong reabsorption of the guided luminescence in large-area LSCs^{10,15}. However, recent breakthroughs in the design of quantum dots have leap-frogged LSC technology to such a degree that they could be commercialized for integrated PV applications in the near future^{7,8,14,16,17}. Colloidal quantum dots feature a broad absorption spectrum that can be tuned to harvest solar radiation across the whole visible spectrum and to the near-infrared (NIR). Their luminescence can be tuned

¹Dipartimento di Scienza dei Materiali, Università degli Studi di Milano-Bicocca, via Cozzi 55, IT-20125 Milano, Italy. ²Glass to Power Srl, Via Monte Nero 66, IT-20135 Milano, Italy. ³Department of Mechanical Engineering, High Temperature and Plasma Laboratory, University of Minnesota, Minneapolis, Minnesota 55455, USA. [†]These authors contributed equally to this work. *e-mail: francesco.meinardi@unimib.it; kortshagen@umn.edu; sergio.brovelli@unimib.it

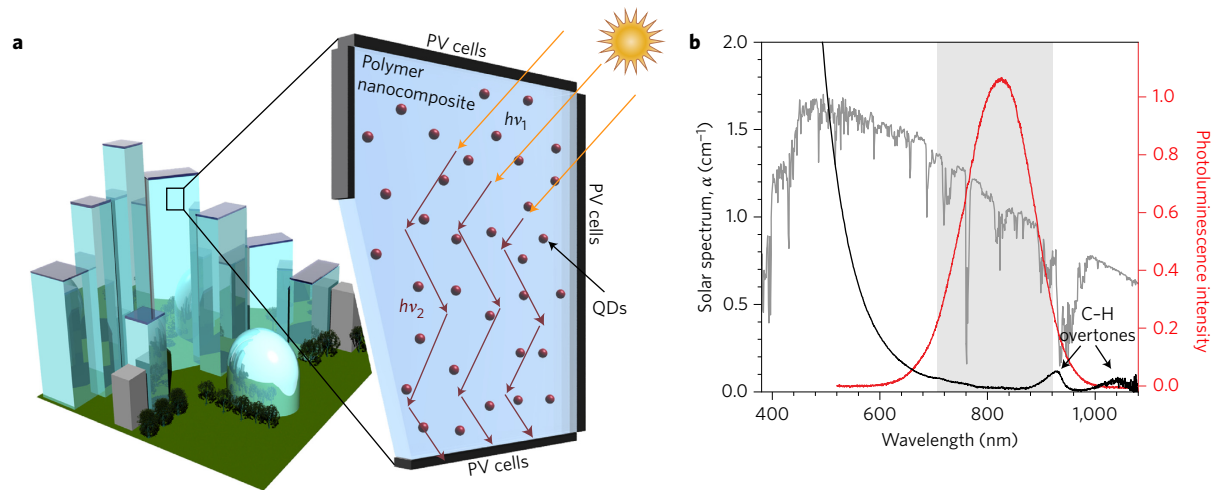


Figure 1 | Concept of LSC window based on ultra-earth-abundant Si quantum dots. **a**, Schematic representation of an LSC window composed of a polymer matrix incorporating reabsorption-free quantum dots (QDs). **b**, Absorption (black line) and photoluminescence (red line) spectra of Si quantum dots (4.3 nm diameter) in crosslinked poly(lauryl methacrylate) (PLMA, QD concentration 0.09 wt%). Photoluminescence was measured using c.w. excitation at 473 nm. The transparency window of the nanocomposite, defined by the absorption onset of the QDs and the C-H overtone of the matrix at 930 nm, is indicated by grey shading. The spectrum of solar radiation at sea level is reported as a grey line.

to match the peak response of PV devices. Most importantly, for the realization of efficient large-area LSCs, the energy separation between the absorption and emission spectra of quantum dots, commonly quantified in terms of a Stokes shift, can be engineered through various material design strategies, including heterostructuring^{7,13,18–21}, doping^{17,22} and the use of ternary semiconductor compositions, leading to intrinsically decoupled absorption and emission functions^{8,23,24}.

One compelling material design concept for achieving reabsorption-free LSCs that is yet to be explored is the use of quantum dots of indirect-bandgap semiconductors such as silicon. In its bulk form, silicon is an indirect-bandgap semiconductor, and light emission from the lowest lying $X_{\text{conduction}} \rightarrow \Gamma_{\text{valence}}$ energetic transition requires the assistance of transverse optical or acoustic phonons, resulting in a vanishingly small transition probability (per atom band-edge absorption cross-section of $\sigma \approx 1 \times 10^{-22} \text{ cm}^{-2}$) and negligible luminescence. However, upon spatial confinement below the exciton Bohr diameter (8.6 nm)^{25–27}, Si nanostructures become strongly luminescent owing to partial relaxation of the selection rules for momentum conservation^{25,28–30}, which confers a small, yet not negligible, oscillator strength to the band-edge electronic transition^{31,32}. In addition to this, recent studies demonstrate that quantum confinement boosts the per atom cross-section of Si with respect of the bulk material, approaching a one order of magnitude enhancement between 2 and 3 eV (ref. 27). This is beneficial for LSC applications, as it enables us to achieve high solar harvesting performances with relatively small quantum dot concentrations. As a result, the optical absorption and photoluminescence spectra of Si quantum dots can be tuned from the visible to the NIR spectral region by control of the particle size ('quantum confinement effect'), and their emission efficiency can be enhanced to >50%^{33,34} via suitable surface passivation strategies^{30,33,35}. For these reasons, Si quantum dots are considered interesting candidates for nontoxic biomarkers³⁶ and for cost-effective solid-state light sources^{37,38}. Importantly for LSC applications, the absorption edge of Si quantum dots retains the very small absorption coefficient typical of indirect-bandgap semiconductors^{31,39,40}, and this results in a negligible overlap between the absorption and emission profiles and, consequently, effective suppression of the reabsorption capability of Si quantum dots.

Another unique and beneficial feature of Si quantum dots that could support the widespread use of LSC technology is that

silicon is the most abundant element on the Earth's crust (Supplementary Fig. 1a). The yearly production of Si is around eight million tons, and only a small percentage of this is sufficient to sustain the demand from the semiconductor and solar energy sectors (the largest part is used in the manufacturing of aluminium and by the chemical industry)⁴¹. The unmatched availability of these raw materials could thus help avoid the issues that affect the applicability of other existing types of Stokes-shift engineered quantum dots to large-scale LSC fabrication. Such quantum dots comprise one or more elements with relatively low abundance in the Earth's crust and that are already heavily used in existing mass production technologies (for example, indium and selenium; Supplementary Discussion and Supplementary Fig. 1b)^{41,42}. Although the yearly production of such elements is sufficient to sustain current global demand, the emergence of a new industrial sector—the large-scale production of quantum dots for building-integrated LSC technology—might lead to supply restrictions and severe price fluctuations.

Here, we use Si quantum dots to realize the first efficient large-area LSC based on indirect-bandgap colloidal nanostructures. The suppressed reabsorption capability of Si quantum dots, together with their high compatibility with polymer matrices, enables us to achieve nearly ideal LSC devices free from reabsorption and scattering. Quantitative performance evaluations, corroborated by Monte Carlo numerical simulations, indicate that these LSCs can be scaled up to larger size without incurring dramatic optical losses due to reabsorption of the guided luminescence. Finally, proof-of-concept flexible LSC prototypes demonstrate the feasibility of PV-active architectural elements with complex curvature, thereby further extending the potential for building integration of LSCs, which could be realized with minimal losses in terms of yearly production of PV electricity with respect to a horizontal flat device.

Synthesis and optical properties of Si quantum dots

Here, we focus on Si quantum dots emitting at 830 nm, synthesized in a non-thermal plasma reactor and subsequently functionalized with 1-dodecene as described previously^{35,43}, but with an additional ultraviolet light treatment to establish photostability of the covalently bonded surface species. Figure 1b reports the optical absorption and photoluminescence spectra of the Si quantum dots (~4.3 nm diameter) embedded in a poly(lauryl methacrylate) (PLMA, see below) matrix used for the fabrication of the LSC waveguides, together with the terrestrial spectrum of solar irradiance. The

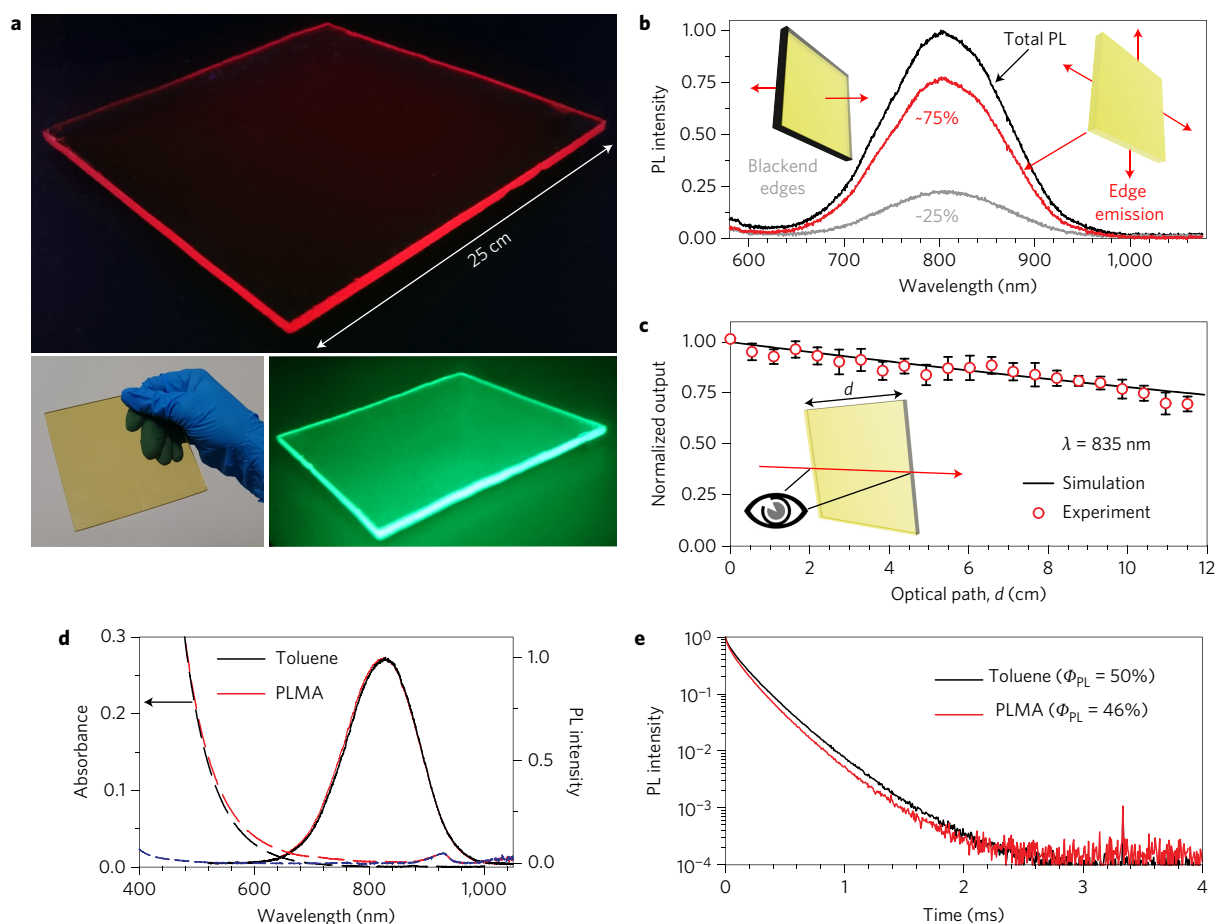


Figure 2 | Large-area LSCs based on mass polymerized nanocomposite waveguides doped with Si quantum dots. **a**, Photographs of an LSC comprising 0.09 wt% Si quantum dots (dimensions of 12 cm × 12 cm × 0.26 cm) under ambient (bottom left) and ultraviolet illumination (365 nm) taken with an ultraviolet-filtered visible camera (top) and an ultraviolet-filtered infrared camera (bottom right). **b**, Photoluminescence spectra of a portion of the same LSC as in **a** (dimensions of 3.5 cm × 3.5 cm × 0.26 cm) with the edges clear (black line) and blocked by black paint (grey line). The red curve is the difference between the black and grey spectra and represents the luminescence emitted from the device edges. **c**, Intensity of 835 nm light linearly propagating inside the LSC in **a** as a function of propagation path d . The light intensity versus d calculated using the Lambert–Beer equation for linear propagation (absorption coefficient α (835 nm) = $2.4 \times 10^{-2} \text{ cm}^{-1}$) is reported as a black line. The error bars are the standard deviation calculated over five repetitive measurements. **d**, Absorption (dashed lines) and photoluminescence (solid lines) spectra of Si quantum dots in toluene (black) and PLMA (red). The absorption spectrum of pure PLMA is shown as a blue dashed line. **e**, Photoluminescence decay curves of the Si quantum dots in toluene and PLMA.

absorption spectrum shows the typical smooth profile of indirect-gap semiconductors³¹ and two small features at 930 and 1,040 nm due to the C–H vibration overtones of the polymer matrix. The photoluminescence spectrum peaks in the optimal transparency NIR window of the composite, which ensures minimal reabsorption losses for large device dimensions, as demonstrated in the following. Because the emission from Si quantum dots is due to a band-edge transition, the real Stokes shift between the absorption and luminescence spectra is zero (Supplementary Fig. 2)^{39,44}. However, because of the partial forbiddance of the $\Gamma_{\text{valence}} \rightarrow X_{\text{conduction}}$ electronic transition, the absorption coefficient of the Si quantum dots below 650 nm is lower than 0.1 cm^{-1} at the quantum dot concentration used (0.09 wt%), which is significantly smaller than the absorption due to the C–H vibration overtones at 930 nm of the LSC waveguide. This results in an effective Stokes shift of $\sim 400 \text{ meV}$, which greatly exceeds that of ‘core-only’ metal chalcogenide quantum dots (typically a few tens of meV)^{7,13,20} and is comparable with the Stokes shift of recently reported reabsorption-free quantum dots^{7,8,17}.

Polymer nanocomposites based on Si quantum dots

To validate experimentally the suitability of Si quantum dots for efficient large-area LSCs, we proceeded with the fabrication of

semitransparent prototype devices using PLMA crosslinked with ethylene glycol dimethacrylate (EGDM) following the procedure described in the Methods. Figure 2a presents a set of photographs of a fabricated rigid P(LMA-co-EGDM) nanocomposite (LMA:EGDM 80%:20% wt/wt) with dimensions of 12 cm × 12 cm × 0.26 cm comprising 0.09% wt% quantum dots. The picture taken under ambient illumination (bottom left) highlights the high optical quality of the LSC waveguide. The absence of scattering due to quantum dot agglomeration and structural defects in the composite is further emphasized by the photographs collected under ultraviolet irradiation with a visible camera (top panel) or an ultraviolet-filtered infrared camera (bottom right), respectively capturing the visible and infrared portion of the quantum dot luminescence. Both pictures highlight that the quantum dot luminescence is effectively guided towards the slab edges, and only a minimal part of the light is emitted from the top or bottom LSC surface.

To quantitatively demonstrate the absence of scattering losses, we performed photoluminescence measurements in an integrating sphere on the same quantum dot–polymer nanocomposite as in Fig. 2a, with either clear or blocked edges so as to distinguish between the light emitted from the LSC faces and the guided luminescence emitted from the slab edges. The photoluminescence

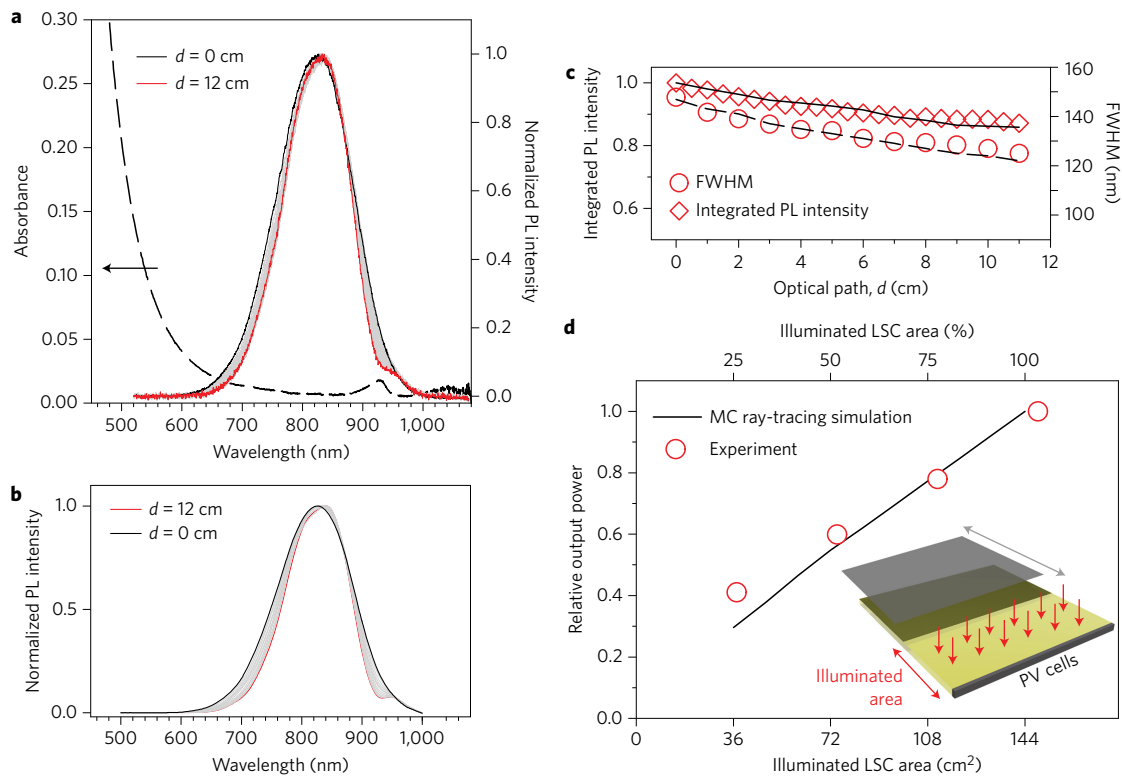


Figure 3 | Large-area QD-LSCs. **a**, Absorption spectrum of the QD-LSC (0.09 wt% Si quantum dots, dimensions of 12 cm \times 12 cm \times 0.26 cm, dashed line) and normalized photoluminescence spectra collected at the edge of the LSC when the excitation spot is located at distances $d = 0$ cm or $d = 12$ cm from the edge. The spectra at intermediate d values are reported as grey curves. **b**, Photoluminescence (PL) spectra versus d calculated through Monte Carlo (MC) ray-tracing simulation. **c**, Full-width at half-maximum (FWHM) and integrated intensity of the experimental and simulated luminescence spectra versus d . **d**, Relative optical output power measured from one LSC edge as a function of device area illuminated by a calibrated solar simulator. The trend obtained through Monte Carlo simulation of an ideal LSC with no scattering/reabsorption losses and embedding emitters with the same quantum efficiency as the Si quantum dots ($\Phi_{\text{PL}} = 46\%$) is reported as a black curve.

data reported in Fig. 2b show that the emission intensity of the LSC with blocked edges corresponds to 25% of the total emission intensity measured for the bare LSC. This leads to the important result that the luminescence guided to the device edges is 75% of the total light generated inside the waveguide, which is in perfect agreement with the maximum theoretical value of light-trapping efficiency defined by Snell's law, $\eta_{\text{tr}} = (1 - 1/n^2)^{1/2} = 0.741$ (where $n = 1.49$ is the refractive index of the polymer matrix), expected for a defect-free waveguide¹⁴ without special reflective coatings (for example, engineered 'selective reflectors') on the top and bottom surfaces of the device. These results further indicate that, in our LSCs, optical losses due to reabsorption are very limited, as isotropic re-emission events would lower η_{tr} by randomizing the propagation path of the guided luminescence¹⁴. A more accurate evaluation of the scattering losses is achieved by light propagation experiments using a collimated laser source at the same wavelength as the quantum dot luminescence (835 nm) entering the device from one edge and collecting the light intensity escaping from the LSC faces. Using the experimental configuration schematized in Fig. 2c, these measurements reveal that the light scattered from the LSC faces is less than 0.6% of the input radiation per centimetre. This loss is over 300 times smaller than the residual absorption by the nanocomposite at 835 nm ($\alpha = 2.4 \times 10^{-2} \text{ cm}^{-1}$, Supplementary Fig. 2). Accordingly, the attenuation of the laser as a function of the optical distance (Fig. 2c) matches perfectly the trend calculated using the Lambert–Beer equation for linear propagation along the waveguide.

One important feature of the fabrication of efficient quantum-dot LSCs (QD-LSCs) is the preservation of the optical properties of the pristine quantum dots following their incorporation into

the polymer nanocomposite. To test the stability of the Si quantum dots to the radical mass polymerization procedure used for the fabrication of the P(LMA-co-EGDM) waveguide, we conducted side-by-side spectroscopic studies of the fabricated nanocomposite and of a toluene solution of Si quantum dots with identical concentration. The optical absorption and photoluminescence spectra are reported in Fig. 2d, which shows virtually identical spectral properties for the two samples (except for the absorption peak at 927 nm due to the vibrational overtone of the C–H stretching mode of the polymer). The absorption spectrum of a slab of pure P(LMA-co-EGDM) with thickness identical to the LSCs is also reported, and shows very low absorption across the visible spectrum and a small peak at ~ 925 nm due to the C–H vibration overtone. The time-resolved luminescence traces in Fig. 2e reveal very similar emission dynamics for the two systems, with a weak acceleration for the Si quantum dots embedded in the polymer that is most probably due to the activation of additional non-radiative channels, which account for the very small reduction in the emission quantum yield from $\Phi_{\text{PL}} = 50 \pm 5\%$ in toluene to $\Phi_{\text{PL}} = 46 \pm 5\%$ in the nanocomposite. Such small non-radiative loss ($\leq 10\%$) upon exposure to the radical polymerization catalysts and energetic ultraviolet radiation in air is particularly notable in light of the fact that the Si quantum dots were not protected with additional passivation coatings, as is necessary to preserve the optical properties of CuInSeS and CdSe quantum dots incorporated into poly-acrylate matrixes (shelled with thick CdS or ZnS layers, respectively)^{7,8}. Measurements performed on one-year-old LSCs show no variation in their emission efficiency and wave-guiding properties. This intrinsic resilience to the device fabrication

conditions is an important industrial advantage of Si quantum dots as it may allow the realization of effective LSC emitters without incurring additional costs for their over-coating.

Reabsorption-free large-area QD-LSCs

We next focus on the quantification of the optical performances of the QD-LSCs. To measure the efficiency of the fabricated concentrator, we index-matched the four perimeter edges ($A_{\text{edge}} = 48 \text{ cm} \times 0.26 \text{ cm} = 12.48 \text{ cm}^2$) of the LSC shown in Fig. 2a to calibrated Si solar cells and illuminated the device perpendicular to its top surface ($A_{\text{LSC}} = 12 \text{ cm} \times 12 \text{ cm} = 144 \text{ cm}^2$) using a calibrated solar simulator with power density $I = 100 \text{ mW cm}^{-2}$ (1.5 AM Global). No reflector or back diffuser was placed at the bottom of the waveguide in order to preserve the optical transmittance of the device and to reproduce the situation of a PV window exposed to sunlight. Based on these measurements, we obtain an optical power conversion efficiency $\eta = P_{\text{out}}/P_{\text{in}} = 2.85 \pm 0.15\%$, where P_{out} is the luminous power collected by the solar cells coupled to the LSC perimeter edges and P_{in} is the solar power incident on the LSC surface. This result is particularly relevant considering the size of the concentrator, its high degree of transparency across the visible spectrum (75%) and the fact that the employed Si quantum dots did not reach maximum luminescence quantum yield ($\Phi_{\text{PL}} = 46\%$). The corresponding optical quantum efficiency, expressed as $\eta_{\text{Q}} = N_{\text{out}}^{\text{ph}}/N_{\text{abs}}^{\text{ph}}$, where $N_{\text{out}}^{\text{ph}}$ is the number of photons emitted from the LSC edges and $N_{\text{abs}}^{\text{ph}}$ is the total number of absorbed photons, is $\eta_{\text{Q}} = 30 \pm 4\%$, which is good agreement with the theoretical value $\eta_{\text{Q}} = \Phi_{\text{PL}} \times \eta_{\text{tr}} \times [1 - \eta_{\text{ra}}] \times [1 - \eta_{\text{s}}] = 35 \pm 6\%$, thus further confirming that the losses due to scattering (η_{s}) and reabsorption (η_{ra}) are particularly small in our LSCs⁶. The obtained power conversion efficiency is comparable to the best performances recently obtained for large-area LSCs with comparable size based on state-of-the-art $\text{CuInSe}_{2-x}\text{S}_x$ quantum dots⁸. We note that it is possible to boost the optical power conversion efficiency of LSCs by using back-reflectors^{10,11,45}, which help recycling transmitted and emitted photons escaping from the waveguide back in the concentrator^{45,46}. In our case, by coupling our LSC to an aluminium-coated silica back-reflector with >95% reflectivity, we obtain $\eta = 4.0 \pm 0.2\%$. The observed ~40% enhancement with respect to the bare LSC is in good agreement with the simulated value of 37% obtained through Monte Carlo ray-tracing calculations. Fundamentally, by using semitransparent back-reflectors, it is possible to enhance the LSC power conversion efficiency while preserving a degree of transparency suitable for application as PV windows.

To directly evaluate the reabsorption losses in our devices, we collected the photoluminescence spectrum from one of the slab edges ($12 \times 0.26 \text{ cm}^2$) using continuous wave (c.w.) 473 nm excitation with the pump spot positioned at different distances d from the waveguide edge. Figure 3a presents the optical absorption spectrum of the LSC of Fig. 2a measured at normal incidence onto the large ($12 \times 12 \text{ cm}^2$) device side, together with the photoluminescence spectra for $d = 0$ –12 cm. The calculated emission spectra obtained using Monte Carlo ray-tracing simulation are reported in Fig. 3b, and nearly perfectly resemble the experimental data. In these calculations, we specifically used the absorption and emission profiles as well as the photoluminescence efficiency ($\Phi_{\text{PL}} = 46\%$) of the quantum dots embedded in the polymer waveguide (Fig. 2d,e). As expected, given the almost complete absence of spectral overlap between the absorption and luminescence profiles of Si quantum dots, the emission spectra excited at the opposite edges of the slab are very similar, with the spectrum for $d = 12 \text{ cm}$ showing only a slight symmetric narrowing with respect to the emission excited directly at the slab edge. Such similar dimming on both sides of the luminescence peak, quantified experimentally and theoretically by the small variation of the spectral linewidth in Fig. 3c, demonstrates that the losses to reabsorption are strongly suppressed

(comparable to the optical losses due to absorption by the C–H vibrational overtone of the matrix) and confirms that the chosen Si quantum dots emit exactly in the optimal NIR transparency window of the nanocomposite waveguide (Fig. 1b). Figure 3c also reports the integrated emission intensity extracted from the spectra in Fig. 3a,b, which enables us to evaluate the losses due exclusively to reabsorption in our devices¹³. The data show a very small drop (~13%) due to reabsorption in 12 cm, which is faithfully predicted by the Monte Carlo ray-tracing simulation. The minimal losses to reabsorption are also in agreement with the quantitative photoluminescence measurements in Fig. 2b, which show that only 25% of the luminescence generated inside the waveguide escapes from the surfaces of the LSC, indicating that randomization of the propagation direction by reabsorption/re-emission processes is very limited.

The effective suppression of luminescence reabsorption by the quantum dots, together with the absence of scattering losses due to the high optical quality of our waveguides (Fig. 2a–c), lead to the ideal situation in which all portions of the LSC surface contribute equally to its total power output. This effect is highlighted in Fig. 3d, where we report the output power extracted from one of the LSC edges ($12 \times 0.3 \text{ cm}^2$) measured using the same set-up adopted for the measurements of η described above (with only one slab edge coupled to the photodiodes and no back-reflector), but progressively exposing increasingly larger portions of the LSC area to the solar simulator. The same figure also reports the expected trend calculated using Monte Carlo ray-tracing simulation for an ideal scattering- and reabsorption-free device of identical dimensions embedded with emitters of the same quantum efficiency as the used Si quantum dots ($\Phi_{\text{PL}} = 46\%$), in which the power output is determined solely by the numeric aperture of the illuminated device area. The experimental data are in very good agreement with the simulated trend, which proves that our LSC is very close to an ideal device. Accordingly, we notice that the light output provided by the first section of the device area (corresponding to one quarter of the total surface) is only 25% larger than the theoretical prediction, in agreement with the small narrowing of the spectral linewidth (~16%) due to limited reabsorption by the quantum dots and by the polymer matrix. This result is further supported by evaluation of the distances travelled by the photons from the primary excitation position to the slab perimeter, calculated by ray-tracing simulations for both experimental and ideal reabsorption-free LSC devices. As reported in Supplementary Fig. 4, the mean photon path length increases by less than 12% (from 8.1 cm to 9.1 cm) in the ideal case, thereby definitively confirming that reabsorption does not significantly alter light propagation in our devices.

Monte Carlo ray-tracing simulations

The calculated optical power conversion efficiency of the bare LSC reported in Fig. 2 ($12 \times 12 \times 0.26 \text{ cm}^3$) obtained by ray-tracing simulation is $\eta_{\text{calc}} = 2.67 \pm 0.17\%$, which is in very good agreement with the experimentally observed value of $\eta = 2.85 \pm 0.15\%$. This enables us to use the experimental device parameters (dimensions, absorption and luminescence spectra, Φ_{PL}) to estimate the optical performances potentially achievable using waveguides of increasingly larger area or slab thickness. Figure 4a,b presents three-dimensional (3D) plots of the optical power efficiency and peak output power, calculated via Monte Carlo ray-tracing simulations with increasing LSC area (from $6 \times 6 \text{ cm}^2$ to $1 \times 1 \text{ m}^2$) and thickness (from 0.25 to 2 cm). The theoretical trend for LSCs with the experimental thickness (0.26 cm) and area ($12 \times 12 \text{ cm}^2$), extracted from the 3D plots, are shown in Fig. 4c,d for clarity. The simulations indicate that $\eta \geq 6\%$ is achievable on increasing the thickness of $12 \times 12 \text{ cm}^2$ devices to 2 cm, which enhances the solar harvesting capability of the experimental LSCs without significant reabsorption

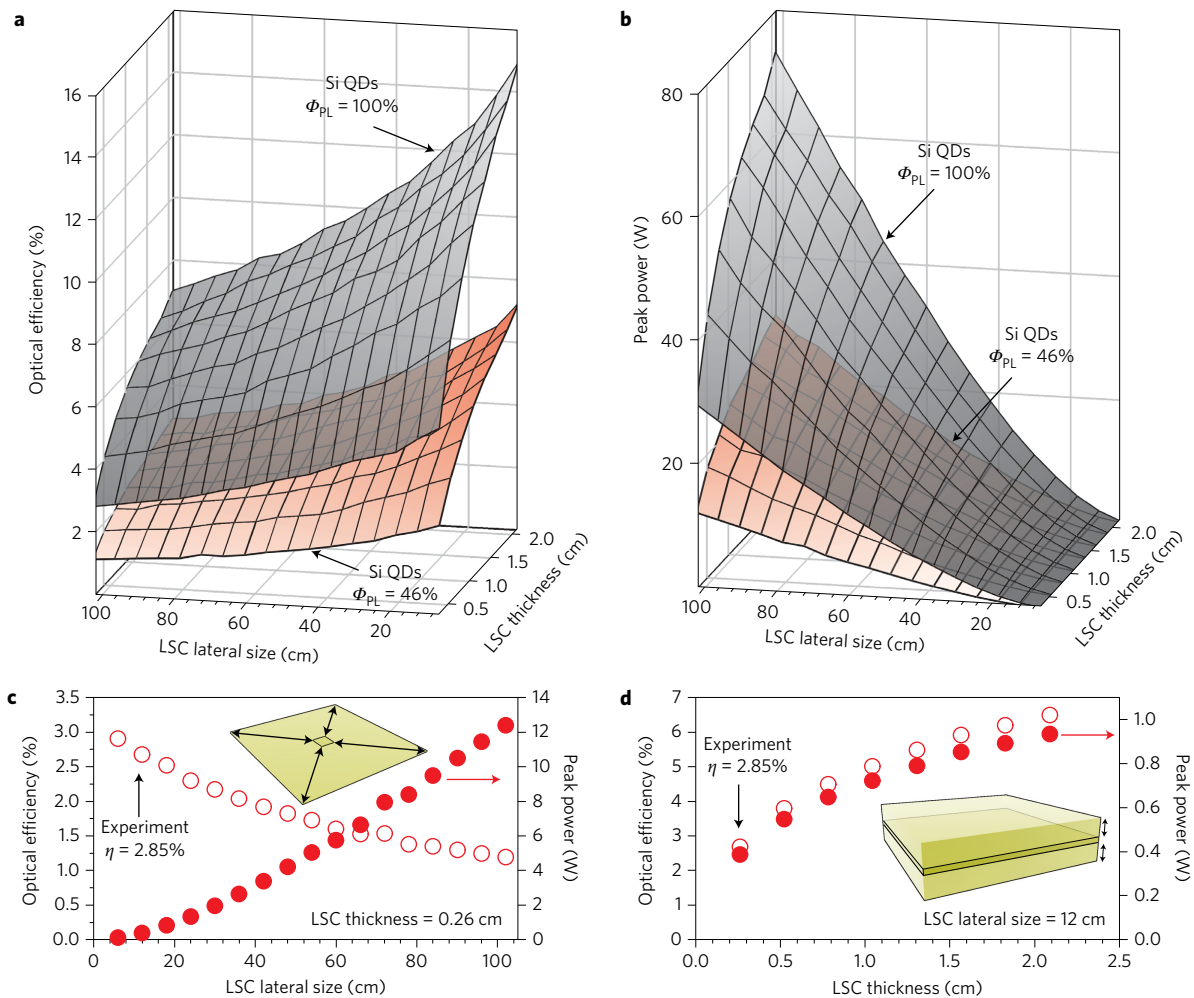


Figure 4 | Monte Carlo ray-tracing simulations. **a,b**, Three-dimensional plots of optical power efficiency η (**a**) and peak power output (at 1.5 AM Global irradiance) calculated through Monte Carlo ray-tracing simulations (**b**) as a function of LSC area and thickness (shaded in red for $\Phi_{\text{PL}} = 46\%$ and in grey for $\Phi_{\text{PL}} = 100\%$). **c,d**, Theoretical trends of η (open circles) and peak power output (filled red circles) for square LSCs with the experimental thickness (0.26 cm) and increasing lateral size (**c**) and the experimental area (lateral size $12 \times 12 \text{ cm}^2$) and increasing slab thickness (**d**) (in both cases $\Phi_{\text{PL}} = 46\%$).

losses (considering the same quantum dot concentration in the final slab). Increasing the LSC area to one square metre leads to the expected mild reduction of the optical efficiency due to the combined effect of weak reabsorption and scattering losses (respectively 1.1% and 0.6% per cm). However, the optical efficiency is preserved at larger than 3% for 2-cm-thick slabs (Fig. 4a,c), and the device peak power output increases with the LSC dimensions, reaching over 30 W for the largest and thickest simulated waveguide (Fig. 4b).

To estimate the ultimate device performances achievable using these LSCs, we also simulated the situation in which the emission efficiency of the Si quantum dots reaches the fully optimized value $\Phi_{\text{PL}} = 100\%$. In this regard, we highlight that a recent study by Linnros and co-workers⁴⁷ has made a critical step towards this fundamental milestone for LSC technology, by reporting colloidal Si quantum dot ensembles with external $\Phi_{\text{PL}} = 70\%$, which is among the highest efficiencies reported for Stokes shift engineered quantum dots emitting in the NIR spectral region^{8,20}. Size-selective photoluminescence measurements by the same authors further demonstrate unity internal Φ_{PL} over a broad range of emission wavelengths⁴⁷, indicating that the deviation from the ideal emission efficiency is due to a relatively small subpopulation of ‘dark’ or blinking quantum dots, rather than to non-radiative processes affecting the whole quantum dot ensemble. This suggests that perfectly emissive Si quantum dots could be achieved by increasing

the fraction of bright particles through suitable passivation strategies. Our calculations, shown in grey in Fig. 4a,b, indicate that $\eta = 15\%$ would be obtained by increasing the thickness of the experimental $12 \times 12 \text{ cm}^2$ LSC to 2 cm (corresponding to approximately 35% transparency in the visible spectral region) and that efficiency as high as $\eta = 7\%$ would be achieved even for the $1 \times 1 \text{ m}^2$ device, which would therefore generate over 70 W of peak optical power. Interestingly, we note that increasing the quantum dot luminescence efficiency from $\Phi_{\text{PL}} = 46\%$ to $\Phi_{\text{PL}} = 100\%$ enhances the calculated LSC performances by slightly more than the factor of two expected by doubling the emission probability after the primary absorption. This effect, which is particularly evident for large LSCs, is ascribed to the mitigation of the small reabsorption losses, as demonstrated by the extension of the mean propagation length for larger Φ_{PL} , and by the increased probability to collect light resulting from more than one absorption event (Supplementary Figs 5 and 6).

Flexible LSCs for curved BIPV elements

We next explore the potential of our QD-LSCs for realizing curved or flexible BIPV elements^{48,49}. To this end, we fabricated tested P(LMA-co-EGDM) rectangular LSCs ($4.5 \times 20 \text{ cm}^2$) doped with Si quantum dots (0.09 wt%) following the same procedure used for the rigid devices in Fig. 2, but selecting a monomer:crosslinker P(LMA-co-EGDM) ratio of 90:10% wt/wt, which yields flexible

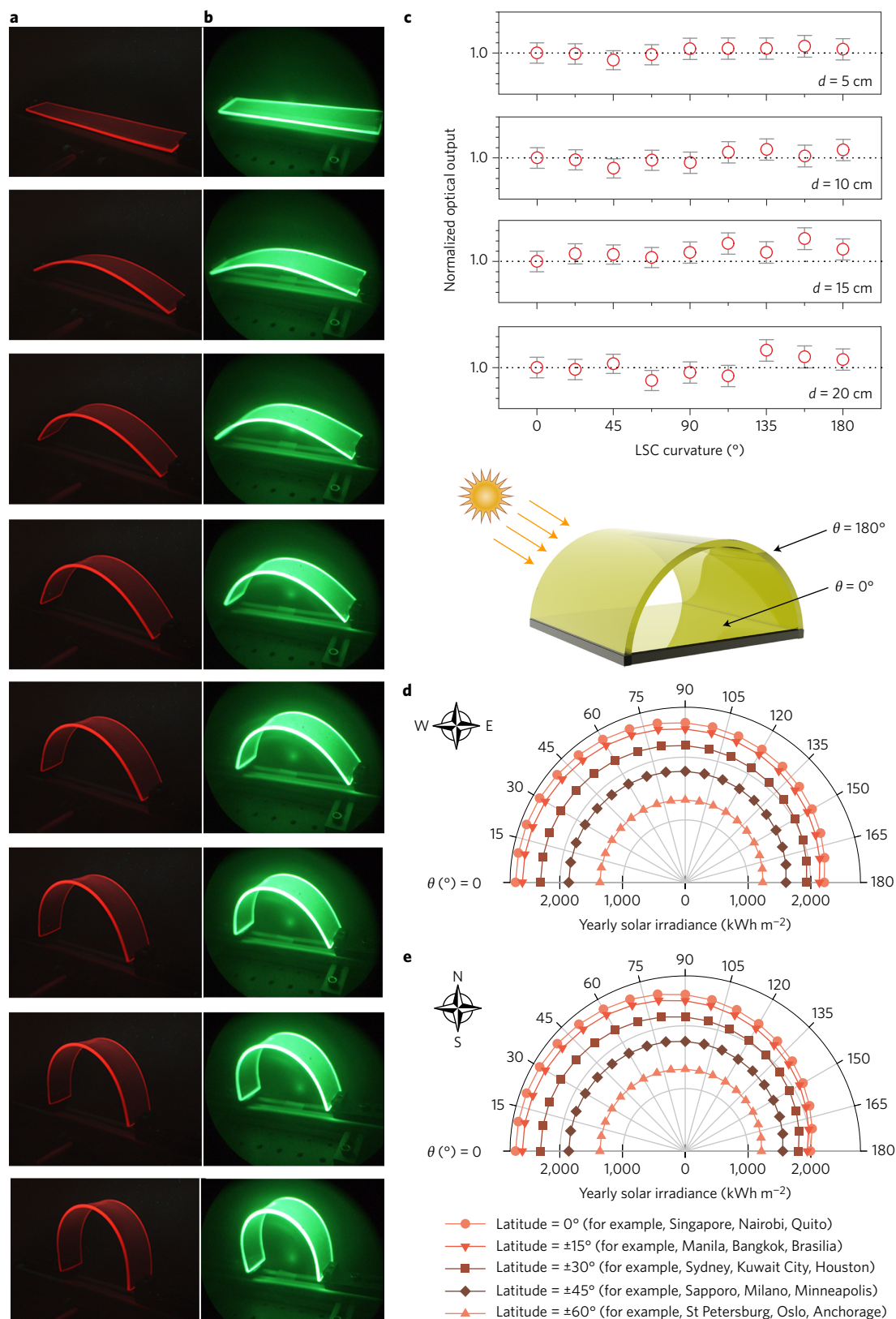


Figure 5 | Flexible QD-LSCs for curved BIPV elements. **a,b**, Photographs of a flexible LSC comprising 0.09 wt% Si quantum dots (LSC dimensions of $4.5 \text{ cm} \times 20 \text{ cm} \times 0.26 \text{ cm}$) under ultraviolet illumination taken with an ultraviolet-filtered visible camera (**a**) and an ultraviolet-filtered infrared camera (**b**). **c**, Optical output as a function of device curvature expressed in terms of the central angle θ for increasing optical distance d between the excitation spot and the slab edge from where the signal is collected. Data are normalized for the intensity at $\theta = 0$. The error bars are the standard deviation calculated over five repetitive measurements. Bottom: schematic representation of a curved LSC with $\theta = 0^{\circ}$ (flat device) and $\theta = 180^{\circ}$ (arch-like structure). **d**, Total yearly solar irradiance in kWh per square metre as a function of θ for a curved LSC in east-west orientation (azimuth angle) at different latitudes (representative geographic locations are reported in correspondence to each latitude). **e**, The same plot for a device in south-north orientation.

waveguides that can be easily bent from flat to semi-cylindrical configurations. Images of the LSC with increasing bending under ultraviolet illumination are presented in Fig. 5a. Figure 5b shows corresponding photographs collected with an ultraviolet-filtered infrared camera that captures the infrared portion of the luminescence spectrum. Both sets of pictures highlight the good optical quality of the flexible device, which, similar to the rigid LSC in Fig. 2, shows light emission primarily from its edges.

To experimentally quantify the effect of curvature on the waveguiding properties of the flexible LSC, we measured the light output from one of the small slab faces ($4.5 \text{ cm} \times 0.26 \text{ cm}$) for increasing spatial separation d between the excitation spot and the LSC edge. The light propagation measurements were repeated under identical conditions of normal excitation and collection geometry for increasing LSC curvature, which we quantify in terms of the central angle θ (with $\theta = 0^\circ$ for a flat device and $\theta = 180^\circ$ for an arch-like structure). For each value of θ , we also conducted Monte Carlo ray-tracing simulations based on the experimental device parameters (dimensions, absorption and photoluminescence spectra and $\Phi_{\text{PL}} = 46\%$) in order to compare the experimental results to the predicted theoretical trends. The normalized optical output data as a function of θ for $d = 5, 10, 15$ and 20 cm are reported in Fig. 5c, showing essentially constant output for all θ , which demonstrates that the waveguiding property of the LSC is unaffected by the device curvature (see Supplementary Fig. 7 for visualization of the Monte Carlo simulations). The invariance of the optical output as a function of θ suggests that our LSCs could be used for the fabrication of semi-transparent PV architectural elements of complex curvature (such as rounded skylights, domes, spherical caps and tiles) without incurring optical losses due to reduced waveguiding ability. We note that such an expanded building integration capability can be achieved with minimal losses in terms of yearly production of PV electricity with respect to a horizontal flat device. This effect is shown in Fig. 5d,e, where we report the total annual solar irradiance in kWh per square metre as a function of θ for a curved LSC in south–north or east–west orientation (azimuth angle). The largest effect is observed at the lowest latitudes, where the maximum drop in the yearly irradiance for a curved LSC with respect to a horizontal device ($\theta = 180^\circ$ versus $\theta = 0^\circ$) ranges between 20 and 25% depending on the orientation. The drop decreases gradually to $\sim 10\%$ with increasing latitudes up to 60° .

Conclusions

We have realized the first example of an LSC based on indirect-bandgap colloidal nanostructures composed exclusively of ultra-earth-abundant materials. By incorporating Si quantum dots into a mass polymerized acrylic matrix, we have fabricated high-optical-quality waveguides that, owing to the large effective spectral separation between the optical absorption and luminescence spectra of the quantum dots, are essentially unaffected by optical losses due to reabsorption of the guided luminescence. As a result, the fabricated devices exhibit power conversion efficiencies as high as 2.85% (corresponding to an optical quantum efficiency of 30%), despite their large area (144 cm^2) and high degree of transparency across the visible spectrum (70% transmittance), which renders them good candidates for the realization of BIPV elements such as PV windows. Furthermore, these LSCs behave as nearly ideal devices, in which all portions of the illuminated surface contribute equally to the total power output. Monte Carlo ray-tracing simulations enabled us to model the optical performances of the LSCs for increasing lateral dimensions and slab thickness; this indicated that a peak power output as large as 70 W could be achieved using slabs with an area of one square metre embedded with optimized Si quantum dots with unitary photoluminescence quantum yield. We also fabricated and tested self-standing flexible LSCs with the aim of evaluating the effects of bending on the waveguiding

properties and thus to assess the suitability of such devices for the realization of PV-active architectural elements of complex curvature. Light propagation experiments corroborated by numerical modelling data indicate that the LSC performances are independent of device curvature, similar to what is observed with plastic optical fibres. These results extend the building integration ability of LSCs, and yearly solar irradiance estimations as a function of LSC curvature indicate that such applications could be realized with minimal losses in terms of yearly production of PV electricity with respect to a horizontal flat rooftop.

Methods

Methods and any associated references are available in the [online version of the paper](#).

Received 19 August 2016; accepted 4 January 2017;
published online 20 February 2017

References

1. Fraunhofer Institute for Solar Energy Systems (ISE). *Current and Future Cost of Photovoltaics. Long-Term Scenarios for Market Development, System Prices and LCOE of Utility-Scale PV Systems*. Report No. 059/01-S-2015/EN (2015).
2. The European Parliament and the Council of the European Union. Directive 2010/31/EU of the European Parliament and the Council on the energy performance of buildings (recast). *Official Journal of the European Union* 23, <http://data.europa.eu/eli/dir/2010/31/oj> (2010)
3. Weber, W. H. & Lambe, J. Luminescent greenhouse collector for solar radiation. *Appl. Opt.* 15, 2299–2300 (1976).
4. Goetzberger, A. & Greube, W. Solar energy conversion with fluorescent collectors. *Appl. Phys.* 14, 123–139 (1977).
5. Debije, M. G. Solar energy collectors with tunable transmission. *Adv. Funct. Mater.* 20, 1498–1502 (2010).
6. Debije, M. G. & Verbunt, P. P. C. Solar concentrators: thirty years of luminescent solar concentrator research: solar energy for the built environment. *Adv. Energy Mater.* 2, 12–35 (2012).
7. Meinardi, F. *et al.* Large-area luminescent solar concentrators based on Stokes-shift-engineered nanocrystals in a mass-polymerized PMMA matrix. *Nat. Photon.* 8, 392–399 (2014).
8. Meinardi, F. *et al.* Highly efficient large-area colourless luminescent solar concentrators using heavy-metal-free colloidal quantum dots. *Nat. Nanotech.* 10, 878–885 (2015).
9. van Sark, W. G. J. H. M. Luminescent solar concentrators—a low cost photovoltaics alternative. *Renew. Energy* 49, 207–210 (2013).
10. Desmet, L., Ras, A. J. M., de Boer, D. K. G. & Debije, M. G. Monocrystalline silicon photovoltaic luminescent solar concentrator with 4.2% power conversion efficiency. *Opt. Lett.* 37, 3087–3089 (2012).
11. Slooff, L. H. *et al.* A luminescent solar concentrator with 7.1% power conversion efficiency. *Phys. Status Solidi Rapid Res. Lett.* 2, 257–259 (2008).
12. Slooff, L. H. *et al.* Long-term optical stability of fluorescent solar concentrator plates. *Phys. Status Solidi A* 211, 1150–1154 (2014).
13. Krumer, Z. *et al.* Tackling self-absorption in luminescent solar concentrators with type-II colloidal quantum dots. *Sol. Energy Mater. Sol. Cell.* 111, 57–65 (2013).
14. Pietryga, J. M. *et al.* Spectroscopic and device aspects of nanocrystal quantum dots. *Chem. Rev.* 116, 10513–10622 (2016).
15. Giebink, N. C., Wiederrecht, G. P. & Wasielewski, M. R. Resonance-shifting to circumvent reabsorption loss in luminescent solar concentrators. *Nat. Photon.* 5, 694–701 (2011).
16. Bomm, J. *et al.* Fabrication and spectroscopic studies on highly luminescent CdSe/CdS nanorod polymer composites. *Beilstein J. Nanotech.* 1, 94–100 (2010).
17. Bradshaw, L. R., Knowles, K. E., McDowall, S. & Gamelin, D. R. Nanocrystals for luminescent solar concentrators. *Nano Lett.* 15, 1315–1323 (2015).
18. Bronstein, N. D. *et al.* Luminescent solar concentration with semiconductor nanorods and transfer-printed micro-silicon solar cells. *ACS Nano* 8, 44–53 (2013).
19. Coropceanu, I. & Bawendi, M. G. Core/shell quantum dot based luminescent solar concentrators with reduced reabsorption and enhanced efficiency. *Nano Lett.* 14, 4097–4101 (2014).
20. Zhou, Y. *et al.* Near infrared, highly efficient luminescent solar concentrators. *Adv. Energy Mater.* 6, 1501913 (2016).
21. Li, H., Wu, K., Lim, J., Song, H.-J. & Klimov, V. I. Doctor-blade deposition of quantum dots onto standard window glass for low-loss large-area luminescent solar concentrators. *Nat. Energy* 1, 16157 (2016).
22. Erickson, C. S. *et al.* Zero-reabsorption doped-nanocrystal luminescent solar concentrators. *ACS Nano* 8, 3461–3467 (2014).
23. Hu, X. *et al.* Ray-trace simulation of CuInS(S₂) quantum dot based luminescent solar concentrators. *Opt. Express* 23, A858–A867 (2015).

24. Knowles, K. E., Kilburn, T. B., Alzate, D. G., McDowall, S. & Gamelin, D. R. Bright CuInS₂/CdS nanocrystal phosphors for high-gain full-spectrum luminescent solar concentrators. *Chem. Commun.* **51**, 9129–9132 (2015).
25. Holmes, J. D. *et al.* Highly luminescent silicon nanocrystals with discrete optical transitions. *J. Am. Chem. Soc.* **123**, 3743–3748 (2001).
26. Hybertsen, M. S. Absorption and emission of light in nanoscale silicon structures. *Phys. Rev. Lett.* **72**, 1514–1517 (1994).
27. Lee, B. G. *et al.* Quasi-direct optical transitions in silicon nanocrystals with intensity exceeding the bulk. *Nano Lett.* **16**, 1583–1589 (2016).
28. Hessel, C. M. *et al.* Synthesis of ligand-stabilized silicon nanocrystals with size-dependent photoluminescence spanning visible to near-infrared wavelengths. *Chem. Mater.* **24**, 393–401 (2012).
29. Mangolini, L. & Kortshagen, U. Plasma-assisted synthesis of silicon nanocrystal inks. *Adv. Mater.* **19**, 2513–2519 (2007).
30. Mangolini, L., Thimsen, E. & Kortshagen, U. High-yield plasma synthesis of luminescent silicon nanocrystals. *Nano Lett.* **5**, 655–659 (2005).
31. Meier, C., Gondorf, A., Lüttjohann, S., Lorke, A. & Wiggers, H. Silicon nanoparticles: absorption, emission, and the nature of the electronic bandgap. *J. Appl. Phys.* **101**, 103112 (2007).
32. Sychugov, I., Pevere, F., Luo, J.-W., Zunger, A. & Linnros, J. Single-dot absorption spectroscopy and theory of silicon nanocrystals. *Phys. Rev. B* **93**, 161413 (2016).
33. Jurbergs, D., Rogojina, E., Mangolini, L. & Kortshagen, U. Silicon nanocrystals with ensemble quantum yields exceeding 60%. *Appl. Phys. Lett.* **88**, 233116 (2006).
34. Anthony, R. & Kortshagen, U. Photoluminescence quantum yields of amorphous and crystalline silicon nanoparticles. *Phys. Rev. B* **80**, 115407 (2009).
35. Anthony, R. J., Rowe, D. J., Stein, M., Yang, J. & Kortshagen, U. Routes to achieving high quantum yield luminescence from gas-phase-produced silicon nanocrystals. *Adv. Funct. Mater.* **21**, 4042–4046 (2011).
36. Erogbogbo, F. *et al.* *In vivo* targeted cancer imaging, sentinel lymph node mapping and multi-channel imaging with biocompatible silicon nanocrystals. *ACS Nano* **5**, 413–423 (2011).
37. Cheng, K.-Y., Anthony, R., Kortshagen, U. R. & Holmes, R. J. High-efficiency silicon nanocrystal light-emitting devices. *Nano Lett.* **11**, 1952–1956 (2011).
38. Ng, W. L. *et al.* An efficient room-temperature silicon-based light-emitting diode. *Nature* **410**, 192–194 (2001).
39. Hannah, D. C. *et al.* On the origin of photoluminescence in silicon nanocrystals: pressure-dependent structural and optical studies. *Nano Lett.* **12**, 4200–4205 (2012).
40. Delerue, C., Allan, G. & Lannoo, M. Electron–phonon coupling and optical transitions for indirect-gap semiconductor nanocrystals. *Phys. Rev. B* **64**, 193402 (2001).
41. Tolcin, A. C. *Mineral Commodity Summaries 2015* (U.S. Geological Survey, 2015).
42. Moss, R. L., Tzimas, E., Kara, H., Willis, P. & Kooroshy, J. *Critical Metals in Strategic Energy Technologies, Assessing Rare Metals as Supply-Chain Bottlenecks in Low-Carbon Energy Technologies* (Joint Research Centre, European Commission, 2011).
43. Wu, J. J. & Kortshagen, U. R. Photostability of thermally-hydrosilylated silicon quantum dots. *RSC Adv.* **5**, 103822–103828 (2015).
44. Wilson, W. L., Szajowski, P. F. & Brus, L. E. Quantum confinement in size-selected, surface-oxidized silicon nanocrystals. *Science* **262**, 1242–1244 (1993).
45. Goldschmidt, J. C. *et al.* Increasing the efficiency of fluorescent concentrator systems. *Sol. Energ. Mater. Sol. Cell.* **93**, 176–182 (2009).
46. Debije, M. G. *et al.* Effect on the output of a luminescent solar concentrator on application of organic wavelength-selective mirrors. *Appl. Opt.* **49**, 745–751 (2010).
47. Sangghaleh, F., Sychugov, I., Yang, Z., Veinot, J. G. C. & Linnros, J. Near-unity internal quantum efficiency of luminescent silicon nanocrystals with ligand passivation. *ACS Nano* **9**, 7097–7104 (2015).
48. Vishwanathan, B. *et al.* A comparison of performance of flat and bent photovoltaic luminescent solar concentrators. *Sol. Energy* **112**, 120–127 (2015).
49. Tummelshammer, C., Taylor, A., Kenyon, A. J. & Papakonstantinou, I. Flexible and fluorophore-doped luminescent solar concentrators based on polydimethylsiloxane. *Opt. Lett.* **41**, 713–716 (2016).

Acknowledgements

S.B. acknowledges the European Community's Seventh Framework Programme (FP7/2007–2013) for financial support (EDONHIST) under grant agreement no. 324603. U.K. and S.E. were supported by the Center for Advanced Solar Photophysics (CASP), an Energy Frontier Research Center funded by the Office of Basic Energy Sciences, Office of Science, US Department of Energy. S.E. also acknowledges support through the NSF Graduate Research Fellowship Program under grant NSF GRFP 00039202. The authors thank M. Acciarri and the staff of the MIB-SOLAR Laboratory for technical assistance with quantitative studies of solar concentration.

Author contributions

The experimental designs were the result of interactions and discussions between S.B. and U.K. S.E. synthesized the quantum dots. L.D. and F.C. fabricated the quantum dot–polymer nanocomposites with the assistance of S.B., R.S. and M.M. S.B. and F.M. planned the experiments. L.D., F.M., F.B. and S.B. performed the spectroscopic experiments and characterized the LSCs. F.M. performed the Monte Carlo simulations. S.B. wrote the paper, in consultation with all authors.

Additional information

Supplementary information is available in the [online version of the paper](#). Reprints and permissions information is available online at www.nature.com/reprints. Correspondence and requests for materials should be addressed to F.M., U.K. and S.B.

Competing financial interests

The authors declare no competing financial interests.

Methods

Materials. Lauryl methacrylate (LMA, 99%, Aldrich) and ethylene glycol dimethacrylate (EGDM, 98%, Aldrich), purified with basic activated alumina (Sigma-Aldrich), were used as monomers for the preparation of polymeric nanocomposites. IRGACURE 651 (BASF) was used as a photoinitiator without purification.

Synthesis of the quantum dots. The Si quantum dots used in this study were synthesized following the procedure reported in ref. 35. Briefly, argon (30 s.c.c.m.) and 5% silane in helium (14 s.c.c.m.) were passed through the length of a borosilicate glass tube reactor with hydrogen injected into the afterglow (100 s.c.c.m.). A nominal power of 45 W at 13.56 MHz was applied via copper ring electrodes placed 4 cm before the afterglow region, where the inner tube diameter expanded from 0.5 to 2 cm. Pressure in the afterglow region was maintained at 1.4 torr by an adjustable orifice downstream of the plasma, after which the hydrogen-passivated Si quantum dots were collected by inertial impaction on glass substrates. These quantum dots underwent hydrosilylation in oxygen-free conditions as described in detail in ref. 43. The quantum dots were dispersed into a 5:1 (vol/vol) mixture of mesitylene and 1-dodecene at a concentration of $\sim 0.8 \text{ mg ml}^{-1}$. The solution was refluxed in a sand bath at 215 °C for 4 h, after which it was stirred while irradiated with a 100 W mercury vapour lamp in excess of 12 h to improve photostability of the quantum dots⁴³. The clear solution was filtered through a 0.2 μm PTFE filter and dried. Excess organic polymers formed during hydrosilylation were removed in a centrifugation washing process with acetonitrile as the antisolvent.

Fabrication of the nanocrystal–polymer composite. As the first step, quantum dot powder was dispersed in a small volume of LMA monomer for 3 h to wet the nanoparticle surface and ensure fine dispersion of the individual quantum dots. The monomer–quantum dot mixture was then added to a large volume of LMA together with a secondary monomer, EGDM (LMA:EGDM 80:20% wt/wt for rigid devices and 90:10% wt/wt for flexible ones) that acts as a crosslinking agent, and a radical photoinitiator (IRGACURE 651; 1% wt/wt). After stirring the mixture for 20 min and sonication for 10 min to facilitate quantum dots dispersion, the homogeneous mixture was poured into a mould made of two low-roughness pieces of tempered glass linked by a PVC gasket, and irradiated with 365 nm light from an ultraviolet lamp for 15 min to trigger radical polymerization. The polymerization was then completed by keeping samples in dark for 40 min while leaving them in the mould to avoid the creation of cracks. After completion of the procedure, the slabs were removed from the mould, cut into pieces of desired sizes, and polished. The slabs were cut using an ultra-thin (0.35 mm), high-precision diamond blade and polished with a Logitech LP50 precision lapping and polishing system.

Thermal characterization of the polymeric nanocomposite. Differential scanning calorimetry (DSC) measurements were performed using a Mettler Toledo DSC1 thermal analysis system equipped with a liquid nitrogen cooling unit for low-temperature operation, calibrated with indium and n-pentane. For each sample, $\sim 8 \text{ mg}$ was sliced and placed in 40 μl Al crucibles. For analysis, we used an initial isotherm of 5 min to thermalize the sample at $-100 \text{ }^\circ\text{C}$, a heating segment from -100 to $60 \text{ }^\circ\text{C}$, followed by cooling to $-100 \text{ }^\circ\text{C}$ and heating to $100 \text{ }^\circ\text{C}$. Each ramp was performed at a rate of 20 K min^{-1} , and followed by a 3 min isothermal equilibration step. Data analysis was performed with Star^e software by Mettler Toledo.

Spectroscopic studies. All spectroscopic studies were carried out using toluene solutions of quantum dots loaded into quartz cuvettes and quantum dot–PLMA nanocomposites. In the measurements of photoluminescence dynamics, the samples were vigorously stirred to avoid the effects of photocharging. The absorption spectra of quantum dot solutions and quantum dot–polymer composites were measured with a Perkin Elmer LAMBDA 950 UV/Vis/NIR spectrophotometer. Photoluminescence spectra and transient photoluminescence measurements were carried out using excitation with $<70 \text{ ps}$ pulses at 3.1 eV from a pulsed diode laser

(Edinburgh Inst. EPL series). The emitted light was collected with a Si charge-coupled device (CCD) camera for the photoluminescence spectra or a Hamamatsu photomultiplier tube (PMT) coupled to time-correlated single-photon counting (TCSPC) electronics (time resolution $\sim 300 \text{ ps}$) for the time decay dynamics. Photoluminescence quantum efficiency measurements were conducted using a c.w. laser source at 473 nm and the same detection set-up coupled to an integrating sphere. Specifically, the sample was mounted vertically at 45° with respect to the incident beam in antireflection geometry with respect to the output window, with the CCD fibre-coupled to the sphere and shielded by a buffer layer. The same set-up was used for the scattering measurements, in which the LSC edges were either clear or blocked using black paint. For light scattering measurements in the linear propagation configuration, 835 nm light from a laser diode was injected into the LSC edge through a 0.5 mm pin hole and the light scattered from the LSC surfaces was collected using a calibrated photodiode. Optical measurements on the LSCs were carried out by coupling the output edge of the slab to an integrating sphere and using a 473 nm c.w. laser as an excitation source. As for the curved LSCs, the excitation beam was kept perpendicular to the slab surface at any curvature to maintain the penetration depth constant for all measurements. Photoluminescence was detected with the same CCD.

Monte Carlo ray-tracing simulation. Simulations of LSC performance were performed using a Monte Carlo ray-tracing method, in which the photon propagation follows geometrical optics laws. Because the LSC thickness is much larger than the light coherence length, the interference has been neglected. The stochastic nature of the simulations is reflected in the fact that the ray is not split upon reaching an interface but rather either transmitted or reflected with the probabilities proportional to the respective energy fluxes given by Fresnel laws. The dependence of these probabilities on the state of polarization of the incident ray (for example, s- or p-polarized) is also taken into account. A specific event (transmission or reflection) is chosen according to random Monte Carlo drawing.

Monte Carlo ray-tracing simulations were performed using the experimental luminescence spectrum and efficiency ($\Phi_{\text{PL}} = 46\%$) of the quantum dots embedded in the polymer waveguide. Furthermore, we used the absorption spectrum of the polymer slab doped with quantum dots to account also for absorption by the polymer matrix.

Inside the LSC material, for each ray, the inverse transform sampling method was applied to randomly generate the length of the optical path before absorption by quantum dots. Path lengths follow the exponential attenuation law determined by the wavelength-dependent absorption cross-section, $\sigma(\lambda)$, and the quantum dot concentration N_{QD} , via an attenuation coefficient, $k(\lambda) = N_{\text{QD}}\sigma(\lambda)$. Because the mean path length, given by the inverse attenuation coefficient, is always much greater than the average distance between quantum dots, there is no need to keep track of an explicit position of each quantum dot, so the LSC material (PLMA + quantum dots) can be considered within the effective medium approach, that is, as a uniform material with the attenuation coefficient defined above.

Once a photon is absorbed by a quantum dot, the subsequent fate of the excitation (that is, re-emission or non-radiative relaxation) is again determined by the Monte Carlo sampling according to the emission quantum yield. The direction of re-emission is distributed uniformly and the re-emission wavelength was determined using the rejection sampling applied to the accurate quantum dot luminescence spectrum obtained from experiment.

The ultimate fate of each photon is either loss due to non-radiative recombination or escape from the LSC via one of the interfaces. A single-ray Monte Carlo simulation was typically repeated 10^5 to 10^7 times to achieve proper statistical averaging. The stochastic nature of simulations allows one to easily evaluate various observables and add additional processes.

Data availability. The data that support the plots within this paper and other findings of this study are available from the corresponding author upon reasonable request.